

Laser Powder Bed Fusion of Reaction-Bonded Silicon Carbide: Process Advancements

W. Declercq¹, S. Meyers¹, J. Vleugels², B. Van Hooreweder¹

¹KU Leuven, Department of Mechanical Engineering, Celestijnenlaan 300,
3001 Heverlee, Belgium

²KU Leuven, Department of Materials Engineering, Kasteelpark Arenberg 44,
3001 Heverlee, Belgium

Abstract

A promising additive manufacturing (AM) process route for reaction-bonded silicon carbide (RBSC) is that of laser powder bed fusion (LPBF) combined with polymer infiltration and pyrolysis (PIP), and liquid silicon infiltration (LSI). The primary benefits of this AM process route over conventional and alternative AM process routes for silicon carbide (SiC) are its enhanced design complexity, fine resolution, near-net-shaping capability, and the absence of a thickness limitation. However, residual silicon and unreacted amorphous carbon persist in the final material, thereby limiting the thermal and mechanical properties. This study investigates two process advancements focused on reducing the amount of these undesired phases. Firstly, the optimization of LPBF through the use of spherical Si powder and the enlargement of the laser spot size are demonstrated to increase the preform relative density after LPBF from 44.7 ± 0.8 vol% to 55.9 ± 0.5 vol%, while simultaneously improving the process productivity by more than an order of magnitude. Secondly, the phenolic resin preparation and curing have been investigated to yield homogeneous carbon characteristics, which better facilitate the reaction into SiC. The resulting RBSC material has an Archimedes density of 2.85 g/cm^3 and demonstrates enhanced mechanical properties (Young's modulus of 266 ± 5 GPa and three-point bending strength of 221 ± 21 MPa) and thermal conductivity ($136 \text{ W/m}\cdot\text{K}$ at room temperature), confirming the viability of this additive manufacturing route for high-performance ceramic applications.

1. Introduction

Silicon carbide (SiC) is a high-performance ceramic material known for its exceptional thermal stability, mechanical performance, and chemical inertness [1]. These properties make it highly suitable for demanding applications across various industries, including thermal protection systems and telescopic mirrors in aerospace, heat exchangers and nuclear components in the energy sector, and wear-resistant tooling and wafer handling components in the semiconductor industry [2].

Conventional manufacturing of SiC components typically follows a powder metallurgy process, where SiC powder is shaped into the desired geometry using a sacrificial polymer binder. Following this, the binder must be removed in a sensitive and time-consuming debinding step, which imposes a maximum thickness constraint to prevent cracking. Final densification is achieved through sintering or liquid silicon infiltration [3,4]. Both debinding and sintering introduce significant shrinkage and potential deformation. Moreover, due to the strong covalent

bonding in SiC, achieving full density via sintering requires extreme temperatures (1900-2200 °C), high pressures (20-50 MPa), and/or sintering additives such as boron and carbon [5-7]. Alternatively, liquid silicon infiltration (LSI) – also known as reactive metal infiltration (RMI) – can densify the component without additional shrinkage [4,8]. In this process, liquid silicon (Si) infiltrates the porous preform by capillary action. The purpose of LSI is twofold: firstly, the liquid Si fills the open porosity, thereby densifying the part; and secondly, it reacts with carbon (C) – originating either from the binder material or an added C source – to form additional SiC via the Acheson reaction: $\text{Si (l)} + \text{C (s)} \rightarrow \text{SiC (s)}$. The resulting reaction-bonded silicon carbide (RBSC) typically contains a residual Si content of 10-20 vol%, which should be minimized to preserve high-temperature performance, as excess Si reduces creep and oxidation resistance [9].

Additive manufacturing (AM) offers a non-traditional shaping route within the general powder metallurgy process [10,11]. Compared to conventional shaping methods such as uniaxial pressing, slip casting, or injection molding, AM enables greater geometric complexity, finer resolution, shorter lead times, and cost-effective small-batch production. Over the past decades, various AM techniques have been explored for fabricating complex SiC components, including stereolithography (SLA) [12-18], binder jetting (BJ) [19-22], material extrusion (ME) [23-27], and laser powder bed fusion (LPBF) [28-32]. While these methods have shown great promise, many rely on high binder content, exacerbating the limitations of debinding and increasing shrinkage.

Meyers et al. [33] introduced an LPBF-based AM route that eliminates the need for a sacrificial binder. This process begins with a mixture of SiC and Si powders. During LPBF, the fiber laser selectively scans the powder bed, melting only the Si particles, which re-solidify to bind the SiC particles. By repeating this process layer by layer, a three-dimensional porous preform can be fabricated. To increase the final SiC content, additional C is introduced inside the pore network through polymer infiltration and pyrolysis (PIP), after which the preform is densified by LSI. This near-net-shape process avoids the drawbacks of the debinding step and the associated shrinkage. However, the relative density after LPBF remains limited to approximately 45 vol%, constraining the final SiC content and resulting in a high residual Si fraction. Additionally, unreacted amorphous C is often retained in the final material. This is attributed to a phenomenon known as "choking," where a dense SiC layer forms around the added C, impeding further reaction due to the low diffusivity of Si and C through SiC. The presence of residual Si and unreacted C greatly limits the thermal and mechanical performance of the final component.

This study presents recent advancements aimed at overcoming these limitations. The primary objective is to *increase the final SiC content by eliminating unreacted C and simultaneously reducing the residual Si content*. In doing so, the thermal and mechanical performance of the final material can be significantly improved while retaining the advantages of the near-net-shaping process. These improvements are achieved through optimization of two critical process steps: (i) the LPBF process and (ii) the PIP process.

For the LPBF process, several strategies are investigated to increase the relative density of the porous preform, as this directly influences the final SiC content. First, irregular Si powder is replaced with spherical Si powder, which improves powder flowability and deposition during LPBF, and enhances powder packing, thereby increasing the relative density. Second, the effect of a larger laser spot size on relative density and LPBF processing window – being the range of

process parameter sets for which successful preforms can be fabricated – is explored. The enlargement of the laser spot size alters the thermal profile of the melt pool and surrounding powder bed, which may increase both relative density and process productivity.

The PIP process is also systematically investigated. Phase fractions are analyzed as a function of the number of PIP cycles. Additionally, the effect of an intermediate heat treatment in between PIP cycles is examined. This treatment allows the existing C to react with the Si binder, creating space for further carbon infiltration in subsequent PIP cycles, thereby increasing the total carbon content and ultimately the final SiC yield. Furthermore, modifications to the phenolic resin formulation and curing cycle are implemented to achieve a more homogeneous carbon distribution and improved reactivity with liquid Si.

2. Materials and methods

2.1 Material fabrication

Dense RBSC cube samples (1 cm³) were fabricated using a four-step powder metallurgy process, as illustrated in Figure 1. The process is detailed below:

1. **Powder preparation:** The feedstock consisted of a powder blend containing 60 vol% SiC (α -SiC, Carborex BW F320, Washington Mills, purity = 99.2%, d_{50} = 29.2 μm) and 40 vol% Si. For the experiments in Section 3.2.1, irregular Si powder (Simet 985, Keyvest, purity 98%, d_{50} = 45 μm) was used, whereas all other experiments used spherical Si powder (Argon atomized, Nanoval GmbH & Co. KG, d_{50} = 25.6 μm). The powders were dry mixed in a polyethylene container using a Turbula multi-directional mixer at 75 rpm for 4 hours to ensure homogeneity.
2. **LPBF:** The SiC-Si powder mixture can be processed on commercial metal-LPBF machines, using for instance a Si wafer as a baseplate. In this study, the layer thickness was fixed to 30 μm , and two different LPBF machines were used:
 - An Mlab cusing machine (Colibrium Additive, formerly Concept Laser GmbH), equipped with a 100 W fiber laser with a wavelength of 1070 nm and a spot size ($1/e^2$) of 50 μm . It was operated under an inert argon (Ar) atmosphere (< 0.3% O₂). Slicing and hatching were performed using Magics (Materialise, Belgium). Continuous scanning strategy was applied with a 90° rotation between layers, and

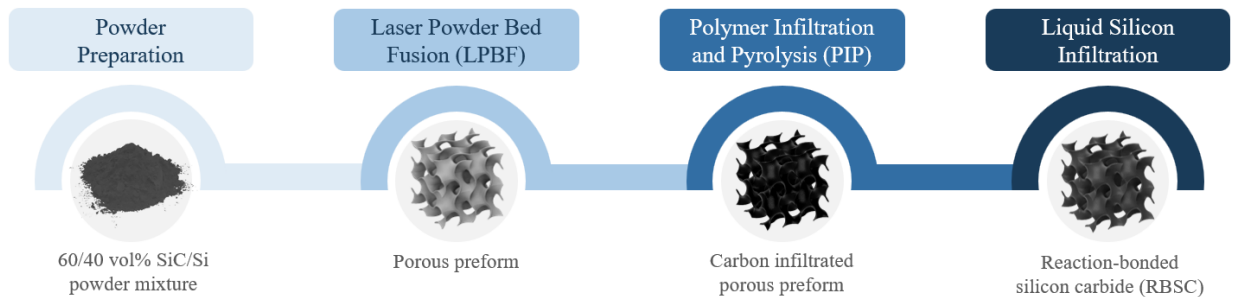


Figure 1: Four-step powder metallurgy process for RBSC, using LPBF as the shaping technology. This process allows the production of highly complex SiC structures, like the gyroid TPMS structure that is used in this illustration.

without contour scanning (fill only). This machine was used for the experiments described in Sections 3.1.1 and 3.2.1.

- A ProX320 DMP machine (3DSystems, Belgium), using a 500 W fiber laser (IPG, Germany) with a wavelength of 1070 nm and a spot size ($1/e^2$) of 90 μm . It was operated under an inert Ar atmosphere (< 25 ppm O_2). Parts were sliced and hatched using 3DXpert (Oqton, Germany). Continuous scanning was applied with a 67° rotation between layers, and without contour scanning (fill only). This machine was used for the experiments described in Sections 3.1.2, 3.2.1, and 3.2.2.
3. **PIP:** The porous SiC-Si preforms were subjected to multiple PIP cycles to introduce C into the porous network. In this study, an in-house prepared phenolic resin was used as the carbon source. The resin constituents were formaldehyde (37 wt% aqueous solution, stabilized with 5-15 % methanol, Acros Organics NV), phenol (purity = 99.5 %, loose crystals, unstabilized, Acros Organics NV), and β -naphthol (2-naphthol, purity = 99+ %, Acros Organics NV). These components were mixed in a glass beaker using a magnetic stirrer-heater at 50°C and 700 rpm until homogeneous, then cooled to 40°C before adding a 3 M NaOH aqueous solution as a catalyst.

Resin infiltration was performed by submerging the preforms until air bubble release ceased. Curing and pyrolysis were conducted in a horizontal tube furnace under an inert nitrogen (N_2) atmosphere. The experiments in Section 3.2.1 used a phenol-to- β -naphthol ratio (P:B) of 2:1, a formaldehyde-to-(phenol + β -naphthol) molar ratio (F:PB) of 2:1, and a (phenol + β -naphthol)-to-catalyst molar ratio (PB:C) of 11:1. The thermal cycle consisted of heating at $5^\circ\text{C}/\text{min}$ to 150°C (3 h dwell), then $2^\circ\text{C}/\text{min}$ to 700°C (2 h dwell), followed by natural cooling. This cycle was repeated multiple times, with an intermediate Si conversion heat treatment performed after one or two cycles. This heat treatment was performed in a vacuum furnace (hot press furnace, W100/150- 2200-50 LAX, FCT Systeme) at 0.1 mbar and involved heating at $50^\circ\text{C}/\text{min}$ to 1050°C , then $10^\circ\text{C}/\text{min}$ to 1450°C , and $5^\circ\text{C}/\text{min}$ to 1500°C (30 min dwell), followed by natural cooling.

For Section 3.2.2, only one PIP cycle was applied without intermediate heat treatment. Before curing, an additional gelation step was performed in a Memmert drying furnace at constant temperature to increase resin viscosity. Thereafter, curing and pyrolysis were conducted in separate steps.

4. **LSI:** The C-infiltrated preforms were placed in boron nitride-coated graphite crucibles, surrounded by chunks of pure Si, and subjected to LSI in a vacuum furnace. For Section 3.2.1, the same furnace and thermal cycle as the intermediate Si conversion heat treatment was used. For Section 3.2.2, a different vacuum furnace (Graphene vacuum furnace, Model PT-V1700-3.4L, Zhengzhou Kejia Furnace Co., Ltd) was used. It was operated at 0.3 mbar, and the thermal cycle consisted of heating at $10^\circ\text{C}/\text{min}$ to 1050°C , then $5^\circ\text{C}/\text{min}$ to 1500°C (30 min dwell), followed by natural cooling.

2.2 Material characterization

The relative density of the porous preforms was calculated from mass measurements and the design volume, assuming a theoretical density of 2.86 g/cm³ based on the 60:40 SiC:Si volume ratio. The pH of the phenolic resins was measured using VWR Prolabo pH test strips.

Final RBSC samples were ground, polished, and examined via optical microscopy (VHX-6000, Keyence). Image analysis (ImageJ) was used to quantify phase fractions. Further phase identification was performed using electron probe microanalysis (EPMA, JEOL JXA-8530F) and X-ray diffraction (XRD, Bruker D2 Phaser). Bulk density was measured using the Archimedes method (Acculab ATL-244-1 with Sartorius YDK01LP kit, using ethanol).

For mechanical testing, RBSC beam specimens ($3 \times 4 \times 45$ mm³) were fabricated and ground to final dimensions according to ASTM C1161-13. Young's modulus was measured using the impulse excitation technique (IET, Grindosonic, Belgium), and three-point bending tests were conducted using an ElectroPuls E10000 (Instron) per ASTM C1161-13. Thermal conductivity as a function of temperature was measured using light flash analysis (LFA 467 HyperFlash).

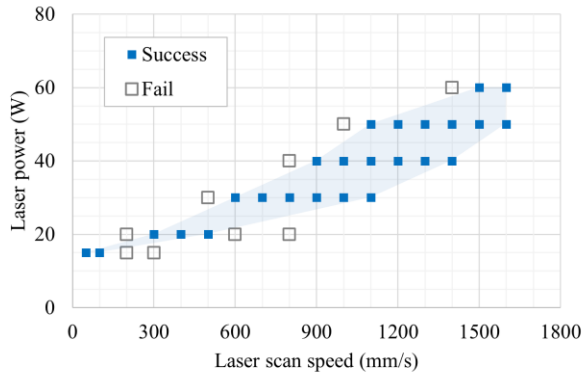
3. Results and discussion

3.1 LPBF process optimization

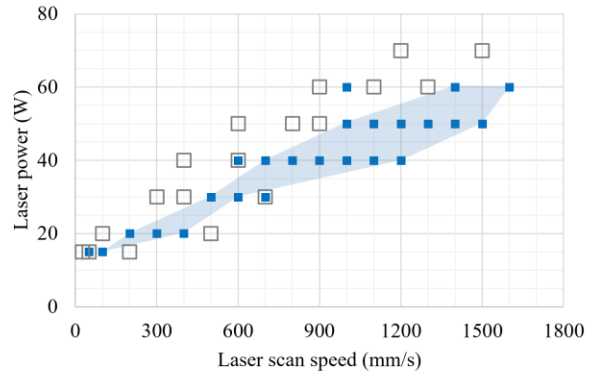
3.1.1 Effect of spherical Si powder

To enhance powder flowability and packing density during LPBF, irregular, milled Si powder was replaced with spherical, gas-atomized Si powder. This morphological change is expected to result in more uniform powder layer deposition and improved relative density of the porous preforms. Figure 2 illustrates the processing windows for varying hatch spacings, highlighting several key process limitations. Firstly, a lower power limit of 15 W is imposed by the minimum stable output capability of the LPBF system. Secondly, a lower scan speed limit – dependent on laser power – is defined by the onset of part failure due to warping from the Si wafer substrate, likely caused by thermal stress accumulation at high energy densities. Thirdly, an upper power limit is imposed by excessive spatter formation above 60 W. Finally, an upper scan speed limit, although less well-defined, is governed by the minimum relative density and structural integrity required for the application, as these properties decrease with decreasing energy density within the processing window. This phenomenon is illustrated in Figure 3, which shows that the relative density of the preform decreases with increasing scan speed for a specific power and hatch spacing.

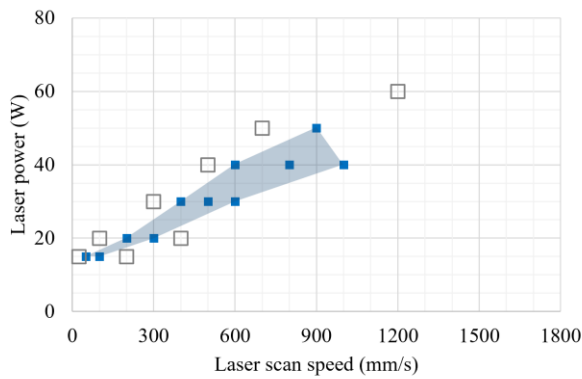
A comparison of the different processing windows, illustrated in Figure 2(d), reveals a leftward shift of the processing window with increasing hatch spacing. Despite this shift, the range of energy densities – defined as laser power divided by the product of hatch spacing, scan speed, and layer thickness – within the processing window remains fairly constant, confirming the importance of the energy density parameter in the determination of the processing window.



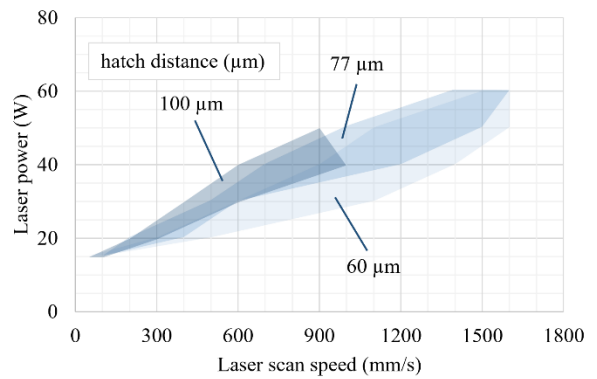
(a) 60 μm hatch spacing



(b) 77 μm hatch spacing



(c) 100 μm hatch spacing



(d) all hatch spacings

Figure 2: Processing windows of SiC-Si powder mixture using spherical Si powder.

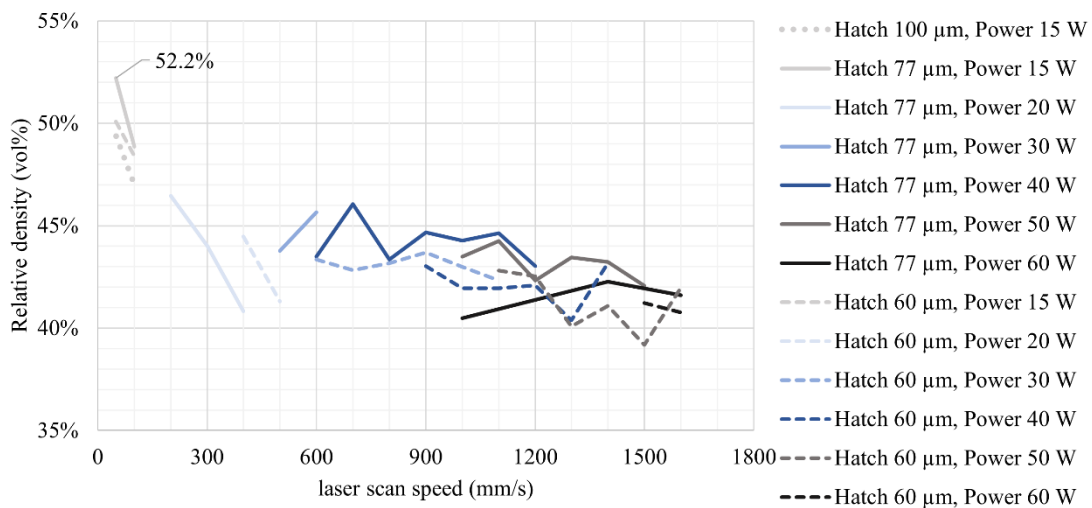


Figure 3: Relative density decreases with laser scan speed for a specific power and hatch spacing.

As illustrated in Figure 4, a downward trend in relative density is observed with increasing laser power, using the scan speed that yielded the highest density – generally the lowest successful scan speed – for each condition. The highest relative density achieved was 52.2 vol% at 15 W, 50 mm/s, and 77 μm hatch spacing. However, this parameter set occasionally resulted in warping, as it lies near the lower scan speed limit. A more robust parameter set – 15 W, 100 mm/s, and 77 μm hatch spacing – yielded a relative density of 48.9 vol%. In comparison, samples fabricated with the same parameters but using irregular Si powder achieved only 44.7 ± 0.8 vol% ($n = 40$), indicating an average improvement of 4.2 vol% due to the spherical powder morphology.

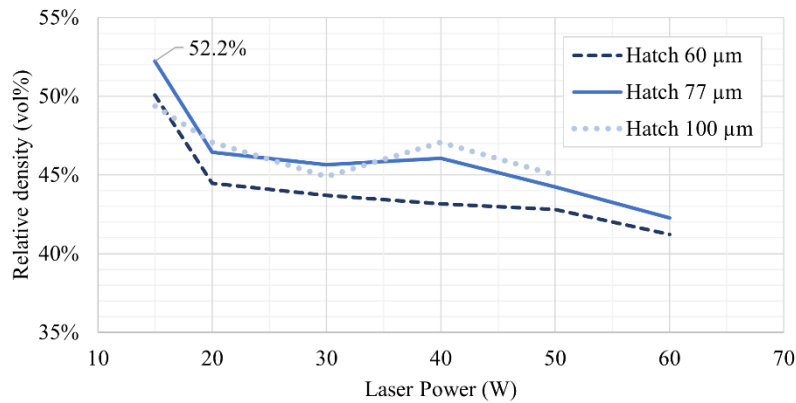


Figure 4: Relative density decreases with increasing laser power.

Despite this improvement, the optimal parameters lie at the lower boundary of the processing window, suggesting that further optimization is possible. One hypothesis is that the small laser spot size results in steep thermal gradients, potentially causing SiC decomposition and limiting the relative density of the porous preforms. This hypothesis will be explored in the following section using a larger laser spot size.

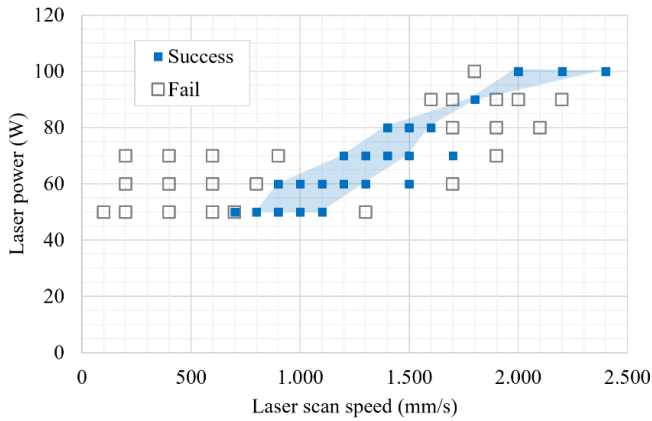
3.1.2 Effect of larger laser spot size

The influence of laser spot size on the LPBF process of the SiC-Si powder mixture was investigated by mapping the processing window on a system equipped with a 90 μm spot size laser, in contrast to the 50 μm spot size used in the previous section. A larger spot size is hypothesized to smooth the thermal gradients within the melt pool and surrounding powder bed, potentially enhancing particle bonding and increasing the relative density of the preform. Additionally, it allows for the use of higher laser power and scan speed combinations without risking SiC decomposition. An added benefit is the potential for significantly increased build rates, thereby improving the productivity of the LPBF step.

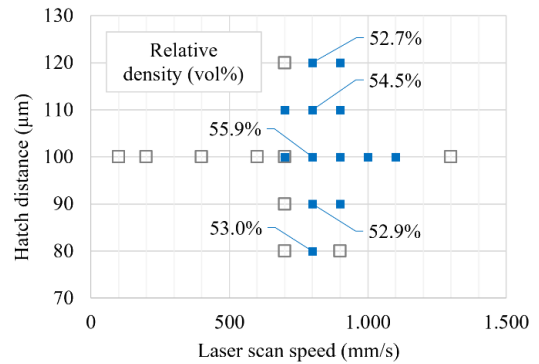
Figure 5(a) presents the processing window for a hatch spacing of 100 μm using the 90 μm spot size. The same processing constraints identified previously – minimum power, scan speed limits, and spatter formation – still apply. The trends in relative density are also consistent, as shown in Figures 5(b) and 5(c), with relative density decreasing at higher scan speeds for a given power and hatch spacing.

The highest relative density achieved with the larger spot size was 55.9 ± 0.5 vol% ($n = 80$), obtained at 50 W laser power, 800 mm/s scan speed, and 100 μm hatch spacing. This represents an average increase of 7.0 vol% compared to the optimal result using the smaller spot size. Moreover, the build rate – calculated as the product of hatch spacing, layer thickness, and scan speed – was 2.40 mm^3/s for this parameter set, compared to just 0.23 mm^3/s for the optimized parameters on the smaller spot size system. In other words, the productivity of the LPBF process was improved by more than an order of magnitude.

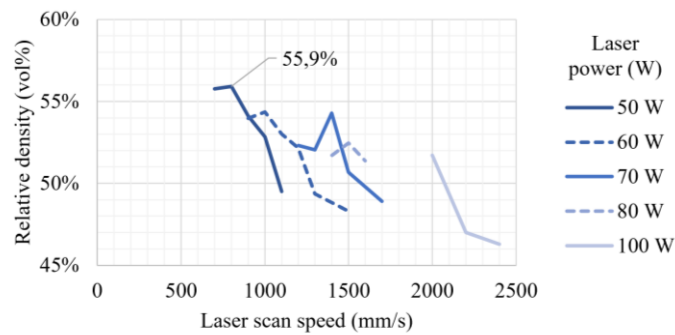
Although the current parameters yield significant improvements, they remain limited by the lower boundary of the processing window. Future research could explore laser beam shaping – such as top-hat, donut, or other multi-mode profiles – to achieve more uniform heating, reduce thermal gradients, and enhance powder consolidation, as this could further increase preform density and build rate.



(a) Processing window for 100 μm hatch spacing



(b) Dependency of processing window on hatch spacing for 50 W



(c) Relative density decreases with laser scan speed for a specific power and hatch spacing

Figure 5: Effect of larger laser spot size on the processing window and relative density trends.

3.2 PIP process optimization

3.2.1 Study of the number of PIP cycles and the effect of an intermediate Si conversion heat treatment

The primary objective of the PIP process is to introduce C into the porous network of the LPBF-fabricated preform, which subsequently reacts with molten Si during LSI to form additional SiC. This section investigates the effect of incorporating an intermediate Si conversion heat treatment between PIP cycles, with the aim of converting the Si binder into SiC and thereby creating additional pore volume for further carbon infiltration. This strategy is intended to increase the total carbon content and ultimately, the final SiC yield.

Figure 6 presents the microstructure of an RBSC sample processed with two PIP cycles, followed by the intermediate heat treatment, two additional PIP cycles, and finally LSI. Phase identification was performed using XRD and EPMA, as shown in Figures 7 and 8, respectively.

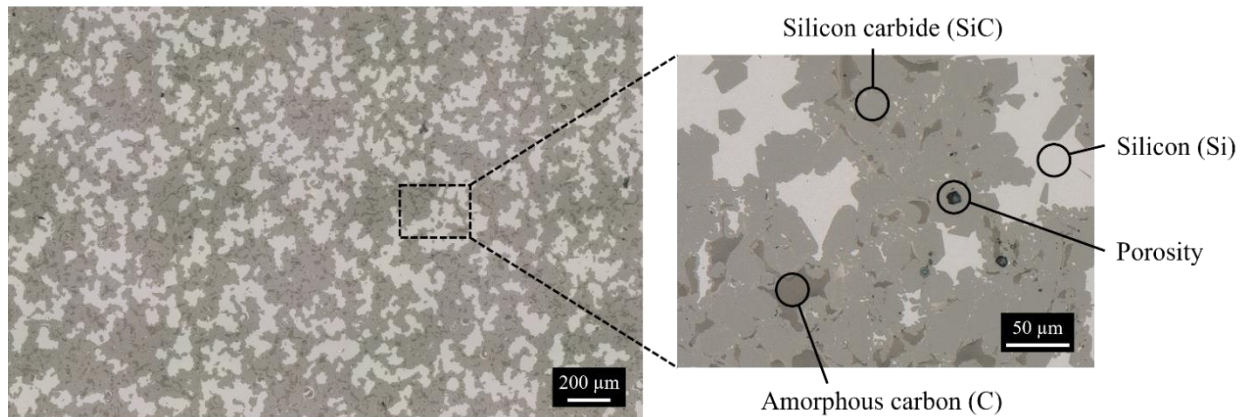


Figure 6: Microstructure of RBSC, via optical microscopy, showing SiC, residual Si, unreacted amorphous C, and few porosities.

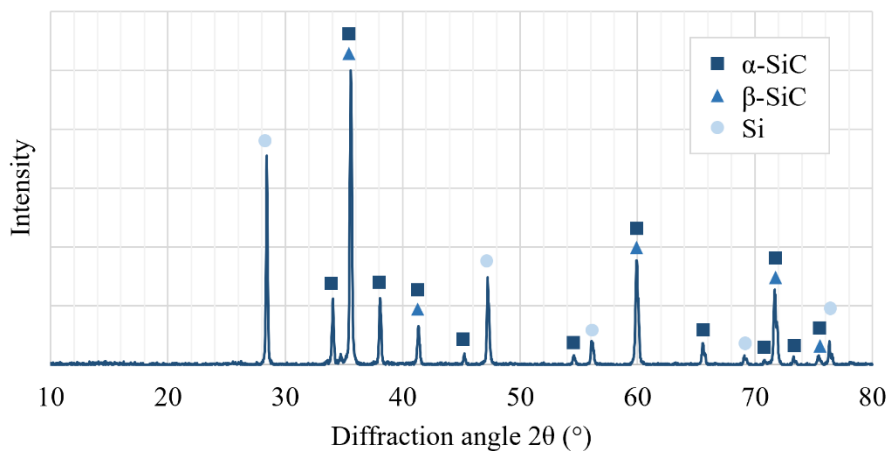


Figure 7: X-ray diffraction pattern of RBSC, showing α-SiC (original powder particles in starting powder), β-SiC (reaction formed SiC during LSI), and residual Si.

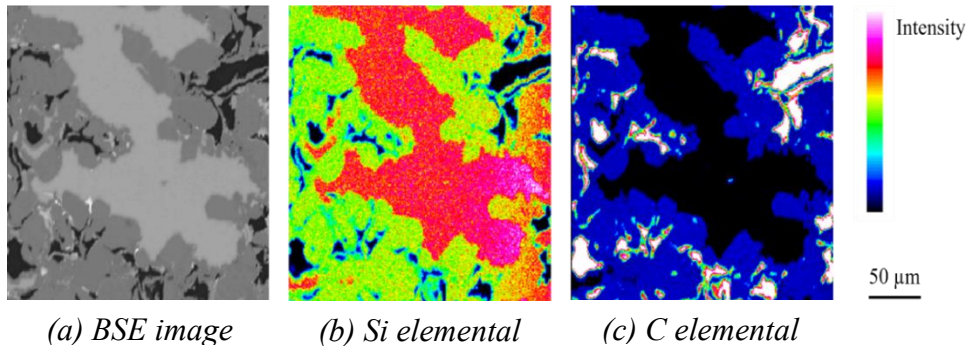


Figure 8: Phase composition analysis of RBSC via EPMA.

The XRD pattern reveals peaks corresponding to residual Si, α -SiC (high-temperature crystal structure originating from the starting powder), and β -SiC (low-temperature crystal structure formed during LSI). It should be noted that the peaks of the two SiC polymorphs coincide, and also differentiation is not possible via optical or electron microscopy. However, the presence of both phases was confirmed by performing Rietveld analysis. The EPMA elemental maps confirm that the dark phase encapsulated by SiC is unreacted C. The absence of diffraction peaks associated with this phase suggests it is amorphous C, consistent with the expected structure of pyrolyzed phenolic resin.

The number of PIP cycles directly influences the amount of C introduced and, consequently, the potential formation of β -SiC. However, excessive PIP cycles can lead to pore choking, resulting in residual porosity. Figure 9 illustrates the evolution of phase composition with increasing PIP cycles and the inclusion of an intermediate Si conversion heat treatment. Interestingly, the SiC fraction increases only marginally – or even decreases – as the number of PIP cycles increases. Instead, the unreacted carbon fraction increases at the expense of residual Si. Although more C is introduced with each cycle, much of it remains unreacted in the final material. This is attributed to the formation of a dense SiC shell ($\sim 10 \mu\text{m}$ thick) at the C–Si interface, which

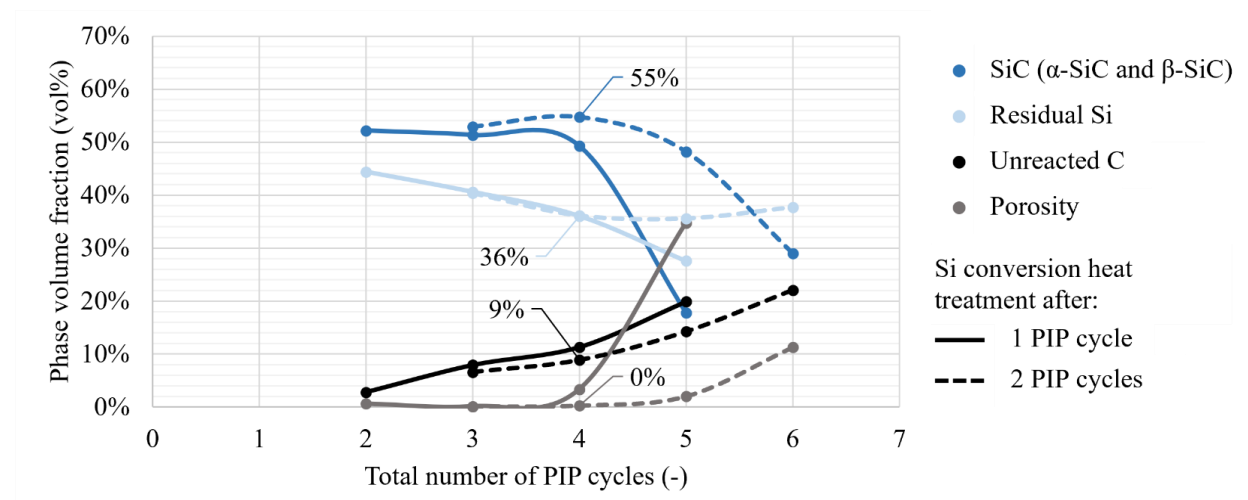


Figure 9: Influence of number of PIP cycles and Si conversion heat treatment on the phase volume fractions in RBSC, measured via image analysis based on optical microscopy.

inhibits further reaction due to the low diffusivity of Si and C through SiC at infiltration temperatures.

At more than four total PIP cycles, the SiC content drops significantly, and substantial porosity is observed, as shown in Figure 10. In these cases, the added C obstructs full Si infiltration by forming dense SiC shells in regions of high local carbon concentration, leading to pore choking. Notably, the measured SiC content in one such sample was only 17.8 vol%, which is lower than the expected 29.3 vol% already present in the porous preform based on the initial powder blend and average relative density. This discrepancy is likely due to breakout porosity introduced during sample grinding and polishing.

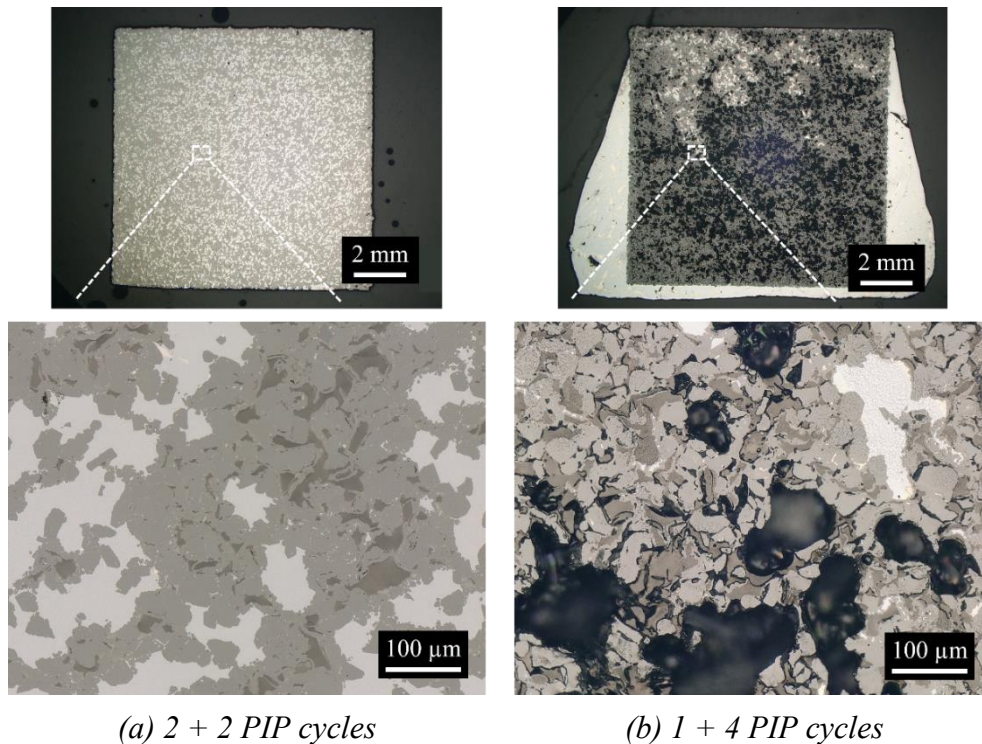
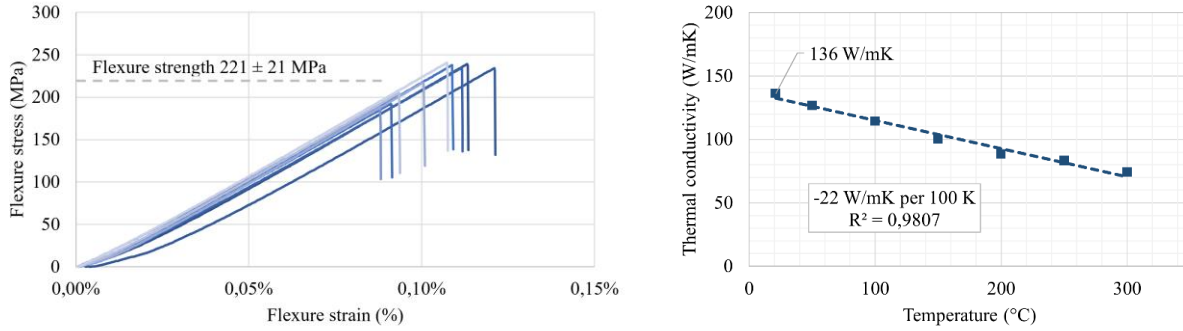


Figure 10: Microstructural analysis of RBSC samples with $x + y$ PIP cycles, x before and y after Si conversion heat treatment.

The highest SiC content was achieved using two PIP cycles before and after the intermediate heat treatment, resulting in 54.7 vol% SiC, 36.1 vol% residual Si, 8.9 vol% unreacted C, and 0.3 vol% porosity. When this same PIP sequence was applied to preforms with higher relative density, fabricated with spherical Si powder and larger laser spot size, the SiC content increased to 62.2 vol%, with 31.8 vol% residual Si, 5.8 vol% unreacted C, and only 0.2 vol% porosity. The corresponding Archimedes density was 2.85 g/cm³, which is consistent with the measured phase fractions.

Further material characterization of this optimized RBSC material is shown in Figure 11. The Young's modulus, measured via IET, was 266 ± 5 GPa, while the three-point bending strength

was 221 ± 21 MPa ($n = 9$). Thermal conductivity at room temperature was $136 \text{ W/m}\cdot\text{K}$, decreasing linearly by approximately $22 \text{ W/m}\cdot\text{K}$ per 100 K up to $300 \text{ }^\circ\text{C}$.



(a) Three-point bending test results

(b) Thermal conductivity test results

Figure 11: Material characterization of RBSC produced by optimal LPBF and PIP processing.

3.2.2 Study of resin formulation and curing heat treatment

While the previous sections focused on optimizing the LPBF and PIP steps, a significant fraction of unreacted C and residual Si remains in the final RBSC material, even under optimal processing conditions. This incomplete carbon conversion during LSI represents an unrealized potential to further increase the SiC content. The composition and thermal treatment of the carbon-yielding polymer – phenolic resin in this case – play a critical role in determining the homogeneity, morphology, and reactivity of the resulting carbon phase within the porous network.

To investigate this, the phenolic resin formulation was varied by adjusting the formaldehyde-to-(phenol + β -naphthol) molar ratio (F:PB) and the (phenol + β -naphthol)-to-catalyst molar ratio (PB:C), while keeping the phenol-to- β -naphthol ratio (P:B) fixed at 2:1. The test matrix is summarized in Table 1. The pH values of the different resin formulations, shown in Figure 12, indicate that pH is primarily influenced by catalyst concentration, independent of the F:PB ratio.

Table 1: Test matrix of phenolic resin compositions.

Phenolic resin	F:PB molar ratio	PB:C molar ratio
F3_C1	3:1	1:1
F3_C8	3:1	8:1
F3_C40	3:1	40:1
F2_C1	2:1	1:1
F2_C5	2:1	5:1
F2_C8	2:1	8:1
F2_C20	2:1	20:1

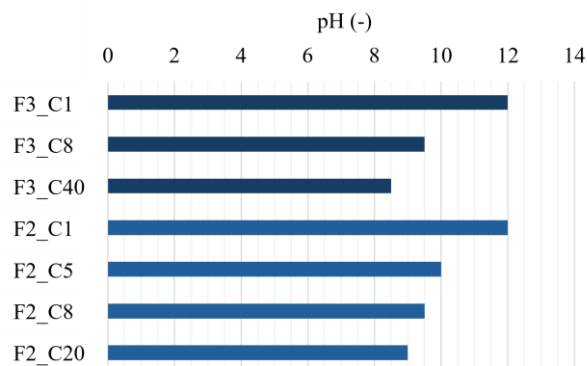


Figure 12: Measured pH of different phenolic resins.

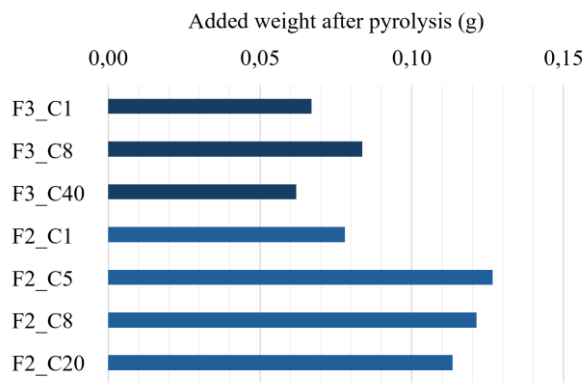


Figure 13: Weight of added carbon to the porous preform after PIP for different phenolic resins.

Each resin was used to infiltrate porous preforms, and the remaining resin was retained for parallel analysis. Both infiltrated and resin samples were placed in a drying furnace for gelation, i.e. the oligomerization of the phenolic resin into short chains, which increases resin viscosity. For the F3 samples, gelation was performed at 60 °C for 20 hours, resulting in moderate viscosities, with F3_C8 showing the highest. For F2 samples, the gelation time was extended to 40 hours, yielding highly viscous or nearly solid samples, except for F2_C1. Interestingly, both C1 resins exhibited low viscosity despite their high catalyst content, likely due to the significant dilution caused by the large volume of 3 M NaOH aqueous catalyst solution added to the resin.

Curing and pyrolysis were conducted in separate cycles. The F3 curing cycle involved staged heating at 50 °C/h to 50 °C (1h dwell), 100 °C (3h dwell), 150 °C (3h dwell), and finally 200 °C (2h dwell), but resulted in bloated, porous samples – likely due to insufficient resin viscosity during water vaporization. For the F2 resins, the heating rate was reduced to 20 °C/h, producing dense, disc-shaped samples. Pyrolysis was performed at 800 °C for 2 hours with a heating rate of 120 °C/h.

The amount of carbon added to the preform after one PIP cycle is shown in Figure 13. Resins that failed to increase viscosity during gelation yielded the lowest carbon additions. F2 resins consistently delivered higher carbon yields than F3 resins, likely due to their closer alignment with the stoichiometric F:PB ratio of 1.67:1. The excess formaldehyde in F3 resins reduces the carbon yield.

After LSI, the resulting RBSC samples were analyzed. Figure 14 compares the microstructures of samples prepared with different phenolic resins. Notably, only F3_C8 and F2_C1 showed complete carbon conversion, with all C reacting into fine SiC grains (0.1-2 µm). In contrast, F3_C1 and F3_C40, despite their relatively low carbon additions, exhibited unreacted C, particularly near the sample edges. This is likely due to insufficient viscosity after gelation, which allowed outward resin movement during thermal treatment, especially during water evaporation. Resins with the highest carbon additions (F2_C5, F2_C8, F2_C20) also showed unreacted C, though F2_C8 was relatively well-converted.

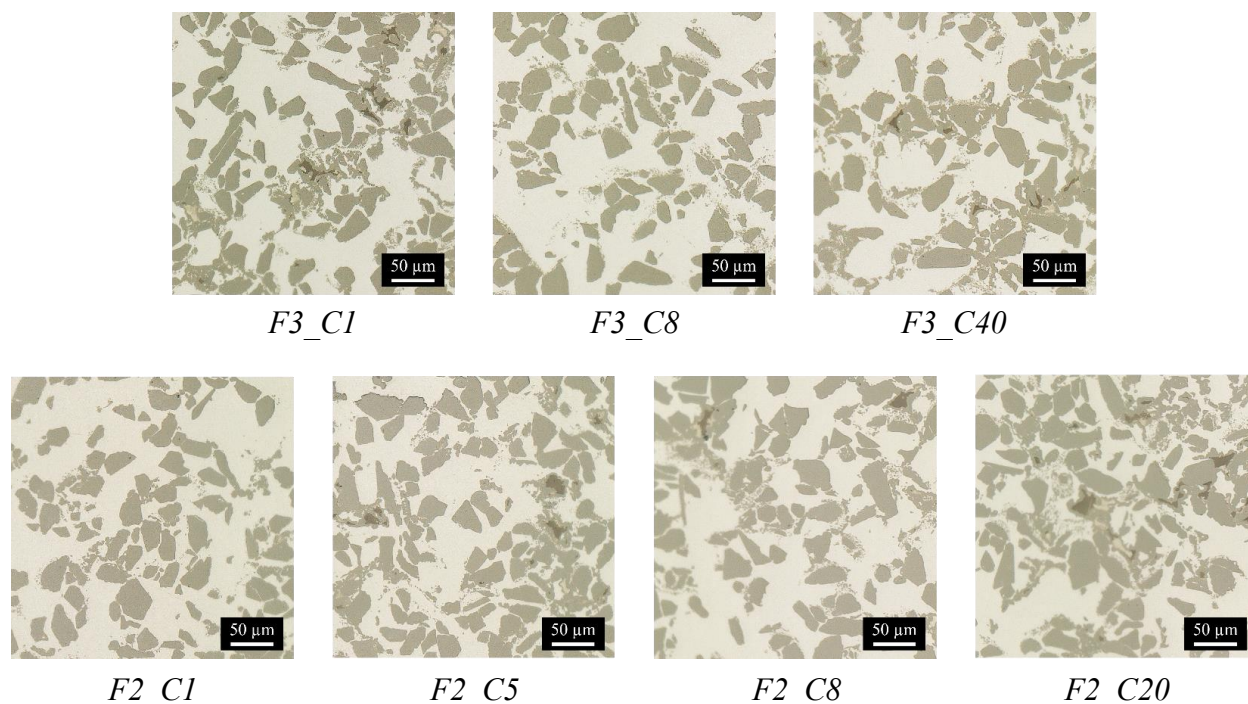


Figure 14: Comparison of RBSC microstructures for different phenolic resins, via optical

The results of phase composition analysis, obtained via image analysis, are shown in Figure 15. The SiC content generally correlates with carbon addition, except for F3_C8, which may be underestimated due to the fine scale of reaction formed SiC grains relative to the resolution of image analysis. Another limitation of the technique is the difficulty in accurately quantifying the unreacted C phase, owing to its insufficient contrast with the SiC phase.

Even after a single PIP cycle, the high-carbon-yield phenolic resins tended to leave unreacted C after LSI. This suggests that achieving both high carbon addition and complete conversion remains challenging. One potential strategy is to explore intermediate F:PB ratios (e.g., 2.5:1) at a PB:C ratio of 8:1. However, the dense carbon structure formed during pyrolysis of

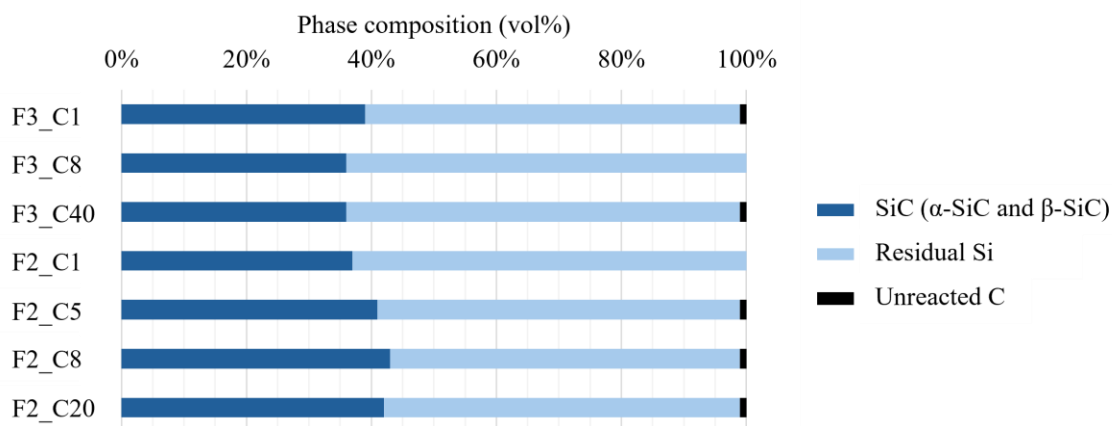


Figure 15: Phase composition of RBSC samples prepared using different phenolic resins.

phenolic resins may inherently limit reactivity due to localized carbon clustering and void formation, particularly after multiple PIP cycles. Therefore, alternative carbon-yielding resins – such as furanic or resorcinol-based systems – may offer more homogeneous carbon distributions and improved morphologies. These characteristics could enhance reactivity with molten Si during LSI, enabling higher SiC fractions in RBSC while reducing or eliminating the presence of unreacted C.

Conclusion

This study presents recent advancements in the LPBF-PIP-LSI process chain for the fabrication of RBSC. The use of spherical Si powder and an enlarged laser spot size during LPBF allowed a substantial increase in preform relative density – from 44.7 ± 0.8 vol% to 55.9 ± 0.5 vol% – and improved process productivity by more than an order of magnitude. These improvements are attributed to enhanced powder flowability, improved packing density, and a more favorable thermal profile during laser scanning. Based on these results, laser beam-shaping is a promising strategy for further optimizing melt pool dynamics, with the potential to simultaneously increase relative density and build rate even more.

In the PIP step, optimization of the number of infiltration cycles and the introduction of an intermediate Si conversion heat treatment enabled a final SiC content of 62.2 vol%, while mitigating pore choking due to excessive carbon addition, resulting in an Archimedes density of 2.85 g/cm^3 . The resulting RBSC material demonstrated enhanced mechanical properties (Young's modulus of 266 ± 5 GPa and three-point bending strength of 221 ± 21 MPa) and thermal conductivity ($136 \text{ W/m}\cdot\text{K}$ at room temperature), confirming the viability of this additive manufacturing route for high-performance ceramic applications.

However, the study of phenolic resin formulation and curing behavior revealed that unreacted amorphous C persists in the final microstructure, even after a single PIP cycle. This highlights the challenge of balancing carbon content and its reactivity during LSI. Adjusting the formaldehyde-to-(phenol + β -naphthol) molar ratio may offer a pathway to improve carbon conversion. But additionally, future research should explore alternative carbon-yielding resins – such as furanic or resorcinol-based resins – which may provide carbon structures with improved reactivity with molten Si, thereby enabling higher SiC content while reducing or eliminating the presence of unreacted C.

Acknowledgments

The authors gratefully acknowledge the support of the European Space Agency (ESA) through the MIMOSA project. Additionally, Waut Declercq acknowledges the financial support of the Research Foundation – Flanders (FWO) through his PhD fellowship for fundamental research (grant number 1130025N).

References

- [1] A. J. Ruys, 'Chapter 2 - Structure and Properties of SiC Ceramics', in *Silicon Carbide Ceramics*, A. J. Ruys, Ed. Elsevier, 2023, pp. 81–163.
- [2] A. J. Ruys, 'Chapter 1 - Introduction and Applications of SiC Ceramics', in *Silicon Carbide Ceramics*, A. J. Ruys, Ed. Elsevier, 2023, pp. 1–79.
- [3] A. J. Ruys, 'Chapter 5 - Direct Sintered (Pressureless Sintered) SiC: DSSC', in *Silicon Carbide Ceramics*, A. J. Ruys, Ed. Elsevier, 2023, pp. 251–347.
- [4] A. J. Ruys, 'Chapter 6 - Reaction Sintered SiC (RSSC)', in *Silicon Carbide Ceramics*, A. J. Ruys, Ed. Elsevier, 2023, pp. 349–394.
- [5] G. Magnani, G. Beltrami, G. L. Minocari, and L. Pilotti, 'Pressureless sintering and properties of α SiC–B₄C composite', *Journal of the European Ceramic Society*, vol. 21, no. 5, pp. 633–638, 2001.
- [6] L. Stobierski and A. Gubernat, 'Sintering of silicon carbide I. Effect of carbon', *Ceramics International*, vol. 29, no. 3, pp. 287–292, 2003.
- [7] J. H. She and K. Ueno, 'Effect of additive content on liquid-phase sintering on silicon carbide ceramics', *Materials Research Bulletin*, vol. 34, no. 10, pp. 1629–1636, 1999.
- [8] P. Sangsuwan, J. A. Orejas, J. E. Gatica, S. N. Tewari, and M. Singh, 'Reaction-Bonded Silicon Carbide by Reactive Infiltration', *Industrial & Engineering Chemistry Research*, vol. 40, no. 23, pp. 5191–5198, 2001.
- [9] N.-L. Zhang, J.-F. Yang, Y.-C. Deng, B. Wang, and P. Yin, 'Preparation and properties of reaction bonded silicon carbide (RB-SiC) ceramics with high SiC percentage by two-step sintering using compound carbon sources', *Ceramics International*, vol. 45, no. 12, pp. 15715–15719, 2019.
- [10] M. Dadkhah, J.-M. Tulliani, A. Saboori, and L. Iuliano, 'Additive manufacturing of ceramics: Advances, challenges, and outlook', *Journal of the European Ceramic Society*, vol. 43, no. 15, pp. 6635–6664, 2023.
- [11] Y. Lakhdar, C. Tuck, J. Binner, A. Terry, and R. Goodridge, 'Additive manufacturing of advanced ceramic materials', *Progress in Materials Science*, vol. 116, p. 100736, 2021.
- [12] W. Li *et al.*, 'Vat photopolymerization of large-aperture high performance SiC mirror through multiphase carbon infiltration modification', *Additive Manufacturing*, vol. 85, p. 104160, 2024.
- [13] X. Guo *et al.*, 'Application of SiO₂-coated SiC powder in stereolithography and sintering densification of SiC ceramic composites', *Ceramics International*, vol. 49, no. 15, pp. 25016–25024, 2023.
- [14] W. Tang, T. Zhao, R. Dou, and L. Wang, 'Fabrication of high-strength Si/SiC composites with low shrinkage rates via vat photopolymerization technology and liquid silicon infiltration', *Additive Manufacturing*, vol. 59, p. 103168, 2022.
- [15] J. Tang *et al.*, 'Preparation of carbon fiber-reinforced SiC ceramics by stereolithography and secondary silicon infiltration', *Ceramics International*, vol. 48, no. 17, pp. 25159–25167, 2022.
- [16] H. Zhang, Y. Yang, H. Kehui, B. Liu, M. Liu, and Z. Huang, 'Stereolithography-based additive manufacturing of lightweight and high-strength Cf/SiC ceramics', *Additive Manufacturing*, vol. 34, p. 101199, 04 2020.
- [17] X. Bai *et al.*, 'Stereolithography additive manufacturing and sintering approaches of SiC ceramics', *Open Ceramics*, vol. 5, p. 100046, 03 2021.

- [18] Q. Fu *et al.*, ‘Silicon carbide whiskers reinforced silicon carbide ceramics prepared by vat photopolymerization and liquid silicon infiltration’, *Ceramics International*, vol. 50, no. 10, pp. 17747–17755, 2024.
- [19] Z. Song *et al.*, ‘Binder jetting 3D printing preparation of SiC ceramics with low free silicon content and densification by PIP and LSI process’, *Journal of Materials Research and Technology*, vol. 36, pp. 5899–5910, 2025.
- [20] P. Chaugule, W. Du, R. Kamath, B. Barua, M. Messner, and D. Singh, ‘Reliability comparisons between additively manufactured and conventional SiC–Si ceramic composites’, *Journal of the American Ceramic Society*, vol. 107, 01 2024.
- [21] K. Feng *et al.*, ‘Bimodal powder optimization in SiC binder jetting for mechanical performance’, *International Journal of Mechanical Sciences*, vol. 274, p. 109278, 2024.
- [22] W. Du, B. Ma, J. Thomas, and D. Singh, ‘Concurrent reaction-bonded joining and densification of additively manufactured silicon carbide by liquid silicon infiltration’, *Journal of the European Ceramic Society*, vol. 43, no. 6, pp. 2345–2353, 2023.
- [23] F. Li, M. Zhu, J. Chen, C. Huang, Y. Zhu, and Z. Huang, ‘High-strength and low-silicon SiC ceramics prepared by extrusion molding 3D printing’, *Journal of the European Ceramic Society*, vol. 44, no. 2, pp. 617–625, 2024.
- [24] J. Best, W. Freudenberg, N. Langhof, and S. Schafföner, ‘Processing-microstructure correlations in material extrusion additive manufacturing of carbon fiber reinforced ceramic matrix composites’, *Additive Manufacturing*, vol. 79, p. 103888, 11 2023.
- [25] L. Wahl, M. Weichelt, P. Goik, S. Schmiedeke, and N. Travitzky, ‘Robocasting of reaction bonded silicon carbide/silicon carbide platelet composites’, *Ceramics International*, vol. 47, no. 7, Part A, pp. 9736–9744, 2021.
- [26] W. Wang, X. Bai, L. Zhang, S. Jing, C. Shen, and R. He, ‘Additive manufacturing of Csf/SiC composites with high fiber content by direct ink writing and liquid silicon infiltration’, *Ceramics International*, vol. 48, no. 3, pp. 3895–3903, 2022.
- [27] A. Held, G. Puchas, F. Müller, and W. Krenkel, ‘Direct ink writing of water-based C-SiC pastes for the manufacturing of SiSiC components’, *Open Ceramics*, vol. 5, p. 100054, 03 2021.
- [28] X. Chen *et al.*, ‘Effect of laser power on mechanical properties of SiC composites rapidly fabricated by selective laser sintering and direct liquid silicon infiltration’, *Ceramics International*, vol. 48, no. 13, pp. 19123–19131, 2022.
- [29] M. Pelanconi, S. Bottacin, G. Bianchi, D. Koch, P. Colombo, and A. Ortona, ‘High-strength Si–SiC lattices prepared by powder bed fusion, infiltration-pyrolysis, and reactive silicon infiltration’, *Journal of the American Ceramic Society*, vol. 107, 02 2024.
- [30] K. Liu *et al.*, ‘Laser additive manufacturing and homogeneous densification of complicated shape SiC ceramic parts’, *Ceramics International*, vol. 44, no. 17, pp. 21067–21075, 2018.
- [31] S. Wu *et al.*, ‘Mechanical characteristics of Si/SiC graded ceramic lattice structures with a triply periodic minimal surface fabricated by laser powder bed fusion’, *Composite Structures*, vol. 346, p. 118417, 2024.
- [32] H. Fu *et al.*, ‘Effect of silicon addition on the microstructure, mechanical and thermal properties of Cf/SiC composite prepared via selective laser sintering’, *Journal of Alloys and Compounds*, vol. 792, pp. 1045–1053, 2019.

- [33] S. Meyers, L. Leersnijder, J. Vleugels, and J.-P. Kruth, 'Direct laser sintering of reaction bonded silicon carbide with low residual silicon content', *Journal of the European Ceramic Society*, vol. 38, 04 2018.